

Observation of banded spherulite in a pure compound by rhythmic growth

Subhadip Ghosh,¹ Dipak Patra,¹ and Arun Roy^{1,*}

¹*Soft-Condensed Matter Group, Raman Research Institute, Bangalore 560080, India*

(Dated: March 18, 2022)

Banded spherulitic growth of crystal is observed in some materials with spherically symmetric growth front and periodic radial variation of birefringence. This variation of birefringence in quasi two dimensional geometry produces concentric interference colour bands when viewed through crossed polarisers. In most materials, the banded spherulites are found to be formed by radially oriented periodically twisted fibrillar crystallites. Here, we report the formation of banded spherulites due to the rhythmic growth of concentric crystallite-rich and crystallite-poor bands for a pure compound consisting of strongly polar rod like molecules. The compound exhibits coexistence of untwisted fibrillar crystallites and an amorphous phase in its most stable solid state. On sufficient supercooling of the sample from its melting point, the banded spherulites are formed with a periodic variation of composition of untwisted radially aligned fibrillar crystallites and an amorphous solid phase. We have developed a time dependent Ginzburg-Landau model to account for the observed banded spherulitic growth.

I. INTRODUCTION

The spherulitic growth of solid is a ubiquitous phenomenon exhibited by many different types of materials such as polymers [1, 2], minerals [3–5], elements [6, 7], metals [8] and salts [9–11]. It is also found in biological materials like coral skeletons [12], kidney stones [13], proteins [14–16] and urinary sediments [17]. In spherulitic growth, the solid phase after nucleation grows with a spherical growth front with continuous orientational symmetry in contrast to the growth of a crystal having discrete orientational symmetries. The spherulites were initially named as “circular crystals” for its circular boundary in quasi two dimensional geometry which changed later to spherulite [18]. In spite of research on it over a century, the detail understanding of the mechanism of this abundantly found natural growth phenomena is still incomplete [8]. The spherulitic growth morphology is often associated with the formation of many radially aligned fibrillar crystallites which branch non-crystallographically for filling space during the growth [19]. This distinct characteristic of spherulites separates it from the other polycrystalline aggregates.

For some materials, the spherulitic growth is accompanied by a series of equidistant concentric bands and is known as banded spherulite. In quasi two dimensional geometry, the banded spherulite domain appears as a flattened disk with circular boundary and these bands appear as concentric circular rings. The polarizing optical microscopic textures of these spherulites show concentric bands with periodic variation of interference colour. Polymers generally form this kind of banded spherulite [1, 2, 8, 20]. Some small molecular systems also produce banded spherulites [21–28]. An organized periodic twisting of radially aligned fibrillar crystallites in the banded spherulitic domain has been observed to generate a peri-

odic change of effective birefringence along the radial direction. This undulation in the birefringence gives rise to concentric bands with periodic variation of colours when viewed through crossed polarisers. In contrast, some multicomponent blends of materials form banded spherulites by rhythmic deposition of host and additive materials [29–31]. Even in some of these cases, twist order of fibrils has been found to contribute to the modulation of effective birefringence along the radial direction. So the organised twisting of the fibrillar crystallites is considered to be a primary mechanism for the formation of the banded spherulites.

In this work, we report the formation of banded spherulite by a pure liquid crystalline compound consisting of relatively small rod-like molecules. We show that the rhythmic growth of concentric crystallite-rich and crystallite-poor amorphous zones is the underlying mechanism for the formation of banded spherulites of this compound contrary to the organised twisting of the fibrillar crystallites. The crystallite-rich zones have higher density of radially aligned fibrillar nano crystallites while crystallite-poor zones are rich in solid amorphous state of the compound. The alternation of these concentric regions changes the effective birefringence periodically along the radial direction of the spherulite giving rise to the concentric interference colour bands between crossed polarisers. We also develop a phase field model to account for the formation of banded spherulite due to rhythmic growth in our system.

II. EXPERIMENT

The commercially available liquid crystalline compound 4'-octyloxy-4-cyanobiphenyl (8OCB) was used with 99% purity. For spherulitic growth, the sample sandwiched between two cleaned coverslips in its isotropic phase was cooled to a desired temperature below its melting point using a microscope hot stage (Linkam). The banded spherulitic domains of the sam-

* aroy@rri.res.in

ple were generally formed above the supercooling $\Delta T = 22.5$ K. The spherulitic domains grown in this way were used for polarising optical microscope (POM) observations and Raman spectroscopic studies. The spacing between the spherulitic bands was determined by taking photographs using a digital camera (Canon EOS 80D) attached to the polarising microscope (Olympus BX50) followed by analysis of the images using the imageJ software.

The micro Raman spectroscopic studies of the spherulite domain were performed using a Raman spectrometer (Jabin-Yvon T64000) equipped with a nano-positioning stage. An air cooled Argon laser (Melles Griot) beam of wavelength 514 nm was used as an excitation source. An objective lens with 50X magnification and 0.75 numerical aperture was used to focus the beam on the sample. The Raman spectra of the sample were recorded from the backscattered light. The theoretically estimated diameter of the focused spot is less than 1 μm .

The field emission scanning electron microscopy (FESEM) studies of the spherulite domain were conducted using the CARL ZEISS (ULTRA PLUS model) system. The banded spherulites of the sample were formed from its melt on cleaned ITO coated glass plates at room temperature. The free surface of these samples was sputter coated with platinum [QUORUM (Q150R S)] for FESEM imaging. For the cross sectional view of the domain, the spherulites formed on coverslips were cleaved in the middle and then the cross sectional areas were sputter coated with platinum for FESEM imaging.

The fluorescent dye (Rhodamine 6G) was mixed with the 8OCB sample at 1:10⁴ wt/wt ratio. The mixture was stirred for 3 hours above the clearing temperature of 8OCB for homogeneous mixing. The sample was then sandwiched between two coverslips and supercooled to room temperature to form the banded spherulites. The fluorescent images of the spherulite domain were captured by a confocal microscope (Leica SP8) equipped with an Argon gas laser. The exciting wavelength was 514 nm.

A DY 1042-Empyrean (PANalytical) X-ray diffractometer with PIXcel 3D detector was used to acquire the X-ray diffraction (XRD) profiles of the sample using $\text{CuK}\alpha$ radiation of wavelength 1.54 Å. The banded spherulites were formed on a cleaned coverslip on cooling the sample to room temperature from its isotropic phase and its formation was confirmed by POM observation. The sample was then scraped off this substrate and placed on a silicon plate. The XRD measurements were performed in the grazing angle of incidence of the X-ray beam. The silicon plate has flat XRD profile which does not interfere with that from the sample.

The temperature variation of dielectric constant of the sample was measured using a homemade setup. The detail of this setup has been discussed elsewhere [32]. A commercially available liquid crystal cell (INTEC Inc.) of sample thickness 5 μm and electrode area 5 \times 5 mm² was used for dielectric measurement. Prior to filling the

sample, the capacitance of the empty cell was measured. The cell was then filled with the sample in its isotropic phase by capillary action on a hot stage. After that, it was supercooled to the lower temperature to form banded spherulite domains. The formation of the banded spherulites was confirmed using POM observation of the sample. A sinusoidal voltage of rms amplitude 0.5 V and frequency 5641 Hz was used for the dielectric measurements. The ratio of the capacitance of the filled cell to the empty cell gives the dielectric constant of the sample.

III. RESULTS AND DISCUSSIONS

The liquid crystalline compound 4'-octyloxy-4-cyanobiphenyl abbreviated as 8OCB exhibits a variety of crystal and liquid crystal phases. The sample shows a melting transition to the smectic A phase at 327.6 K on heating from its most stable crystal phase known as commercial powder or CP phase. On further heating, the compound transforms to nematic and to isotropic liquid phase at 340.1 K and 353.1 K respectively. The sample exhibits a large range of supercooling from its smectic A phase. The banded spherulitic domains are formed on supercooling the smectic phase by at least 22.5 K below the melting temperature. The probability of getting the banded spherulites increases with higher supercooling.

These banded spherulites generally show four black brushes parallel to the polarisers forming a Maltese cross in addition to the concentric interference colour bands between crossed polarisers. These colour bands arise from the periodic variation of the effective birefringence in the sample along the radial direction. Fig. 1a shows a polarising optical microscope (POM) texture of a banded spherulite formed between two coverslips on cooling the sample to room temperature. The black and white appearance of the interference colour bands in this texture is due to relatively lower thickness of the sample with phase retardation in the first order region of the Levy chart. The dark arms of the Maltese cross remain invariant on rotating the sample between crossed polarisers. This implies that the major axis of the effective refractive index ellipse in the plane perpendicular to the light path lies parallel or perpendicular to the radial direction of the spherulitic domain.

The POM studies using a λ -plate (530 nm) were performed to determine the orientation of this major axis. Fig. 1b is the POM image after introducing the λ -plate in the optical path of the microscope. The yellow double headed arrow shows the orientation of the slow axis of the λ -plate with respect to the orientations of the crossed polarisers. It can be inferred from the Levy chart that there is effective addition and subtraction of path differences due to the sample and the λ -plate in the blue and yellow coloured regions of the texture respectively. This observation clearly indicates that the major axis is oriented parallel to the azimuthal direction of the banded spherulite. Hence the spherulite observed for this sam-

ple is optically negative [1, 8]. The white double headed arrows in Fig. 1b show the orientation of the major axis around the seed of this spherulite domain. The spacing between successive bands is also measured for different values of supercooling of the sample and compared with

the theoretical results discussed later. The band spacing does not vary appreciably with the thickness of the sample (see Fig. S1 in the Supplementary Material) which also agrees with our theoretical model.

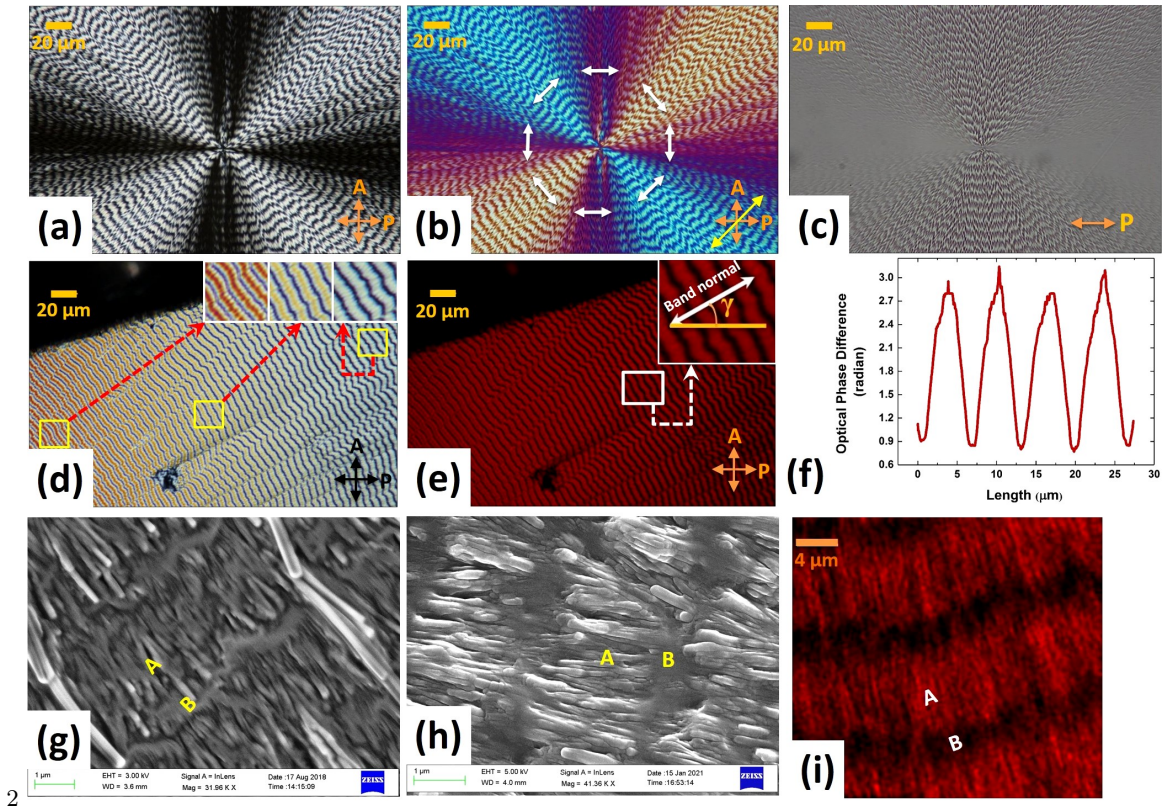


FIG. 1. **Microscopic textures of banded spherulite.** The POM textures of banded spherulite of compound 8OCB at room temperature (a) between crossed polarisers, (b) between crossed polarisers and a λ -plate and (c) with only the polariser in the optical path. The white double headed arrows in (b) indicate the orientations of major refractive index around the seed. (d) The POM texture of a banded spherulite domain between crossed polarisers for relatively thicker sample at room temperature. The insets show the variation of colour in the bands in three different regions with slightly different sample thickness. (e) The same as in (d) with a red filter introduced in the optical path. The inset shows the variation of light intensity along the band normal which makes an angle γ with the polariser. (f) The variation of optical phase difference along the radial direction of the banded spherulite shown in (e). The FESEM image of (g) the top surface of a banded spherulite and (h) the cross-sectional view of a banded spherulitic obtained from the cleaved surface showing the bulk structure. (i) The fluorescent image of a dye doped banded spherulite at room temperature. The regions marked “A” and “B” represent the concentric crystallite-rich and crystallite-poor bands respectively.

Fig. 1c is the bright field image of the sample shown in Fig. 1a with only the polariser in the light path. In this figure, the bands have low (high) optical contrast where band normal is parallel (perpendicular) to the polariser. These observations indicate that the radial component of refractive index does not vary appreciably along the radial direction but the strong variation of the azimuthal component along the radial direction produces the undulation of the birefringence in the spherulite.

For relatively thicker sample, there are multiple interference colour rings in a given spherulitic band as shown

in Fig. 1d. The insets in Fig. 1d are the magnified view of these interference colour rings in three regions with slightly different sample thickness. The variation of phase retardation in the texture can be measured from the intensity variation by introducing a red filter in the light path of the POM. Fig. 1e is the POM image of the spherulite domain with a periodic variation of intensity along the radial direction of the spherulite. The inset in Fig. 1e depicts the magnified view of the marked region of this domain where the band normal makes an angle $\gamma = 30.5^\circ$ with respect to the polariser. Then

the phase retardation can be calculated from the formula $I = I_0 \sin^2(2\gamma) \sin^2(\phi/2) + I_d$, where I_0 , I and I_d are the incident, measured and the dark background intensities with crossed polarisers respectively. The phase retardation $\phi = 2\pi d\Delta n/\lambda$, where d is the sample thickness, Δn is the effective linear birefringence of the sample and λ is the wavelength of incident light. Fig. 1f shows the measured variation of optical phase retardation along the radial direction of the spherulite. The variation of sample thickness for the selected small region shown in the inset of Fig. 1e is negligible and the oscillation of phase retardation across the bands mainly arises due to the variation of the birefringence in the sample.

The field emission scanning electron microscopy (FESEM) studies of the banded spherulite domain showed concentric bands with same periodicity as found in POM studies. The high resolution FESEM texture of the spherulitic domain revealed that it consists of numerous fibrillar nano crystallites embedded in an amorphous phase. The bands in the spherulite arise from the periodic growth of crystallite-rich and crystallite-poor concentric zones as shown in Fig. 1g. Similar repetitive structure was also found in the FESEM texture of the bisected cross sectional surface area of the sample (Fig. 1h) showing its bulk nature (also see Fig. S2 in the Supplementary Material). The FESEM textures of the sample

revealed that the crystallite-rich zones (marked as **A**) have high density of fibrillar crystallites aligned along the radial direction while crystallite-poor zones (marked as **B**) are rich in solid amorphous state of the compound. The crystallites have length similar to the periodicity of the bands while the width varies from 100 nm to 300 nm.

Some polymers and a few small molecular systems exhibit concentric colour banded spherulites [1, 2, 8, 20–25] in which organised twisting of fibrillar units along their long axis has been observed as the mechanism of the band formation. In some small molecular systems, a periodic variation of orientation of individual crystallites has been reported to produce concentric colour bands [33, 34]. But in our sample, neither twist nor periodic change of orientation of fibrillar crystallites is found. The FESEM studies depict that the rhythmic growth of concentric crystallite-rich and crystallite-poor zones produces the banded spherulite of 8OCB. The periodic change in birefringence along the radial direction due to these concentric zones gives rise to the interference colour bands observed between crossed polarisers. The crystallite-poor regions possess least birefringence due to their predominant amorphous nature while the crystallite-rich zones have larger birefringence due to the presence of large number of radially aligned crystallites.

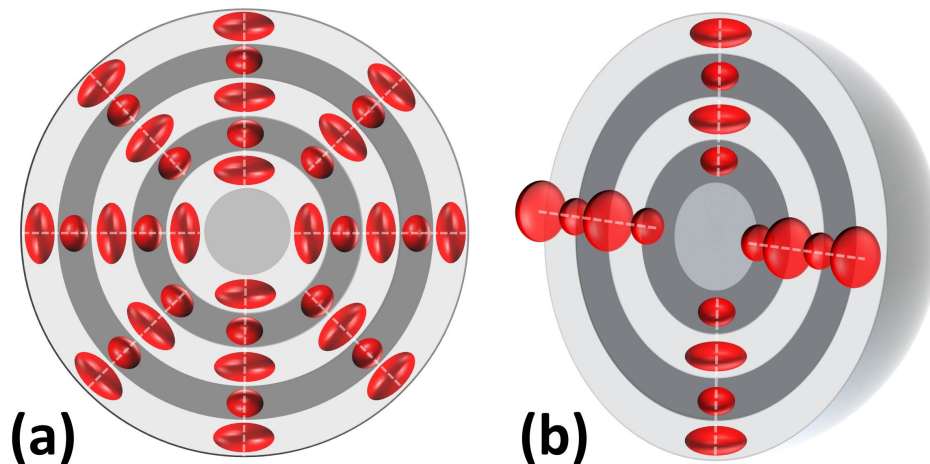


FIG. 2. **Indicatrix ellipsoid in banded spherulite.** The schematic representation of the variation of optical indicatrix along the radial direction of the banded spherulite of the compound 8OCB. The (a) top and (b) side views showing the uniaxial oblate indicatrix with radially oriented optic axes.

A fluorescent image of the banded spherulite domain (see Fig. 1i) was obtained by doping the sample with a fluorescent dye (Rhodamine 6G). It shows a periodic variation of dye concentration along the radial direction of the spherulite domain. The crystallite-rich zones are found to have higher concentration of dye molecules compared to the crystallite-poor zones which

makes these zones brighter and darker respectively in the fluorescent image. The dynamic advection of the dye molecules during the growth of crystallite-rich and crystallite-poor zones perhaps can explain their distribution in the banded spherulite of the sample. The molecular density is higher in crystallite-rich zones compared to crystallite-poor amorphous regions. Thus the growth of

a crystallite-rich band produces a diffusive current which advects the dye molecules from the leading edge of the growth front that gives rise to the higher density of the dye molecules in this band. The depletion of molecular density promotes the formation of crystallite-poor amorphous zones with lower density of the dye molecules. The repetition of these processes leads to the formation of banded spherulite in this sample.

Fig. 2 shows the schematic representation of the variation in the refractive index ellipsoid along the radial direction of the banded spherulite. The FESEM studies revealed that the elliptical or rectangular cross sections of radially aligned fibrillar crystallites are oriented randomly in the banded spherulite giving rise to a uniaxial structure about the radial direction (see Fig. S3 in the Supplementary Material). The POM studies showed that the azimuthal component of the refractive index is larger than the radial component in the spherulite. Hence, the

banded spherulite of 8OCB possesses uniaxial oblate indicatrix with a radially oriented optic axis as shown in Fig. 2. The radial component of refractive index does not vary appreciably along the radial direction but the periodic variation of the transverse component gives rise to the modulation in the birefringence of the sample as observed in Fig. 1c.

The X-ray diffraction (XRD) studies were performed to identify the crystal structure of the banded spherulite domain. The XRD profile (Fig. 3a) of banded spherulite is identical to that of the commercial powder or CP crystal phase of 8OCB. We have recently shown that the CP crystal phase is composed of fibrillar nano crystallites of the compound embedded in its own amorphous solid state [32]. All the peaks observed in the XRD profile are associated with the monoclinic crystal structure of the nano crystallites. The amorphous component shows only

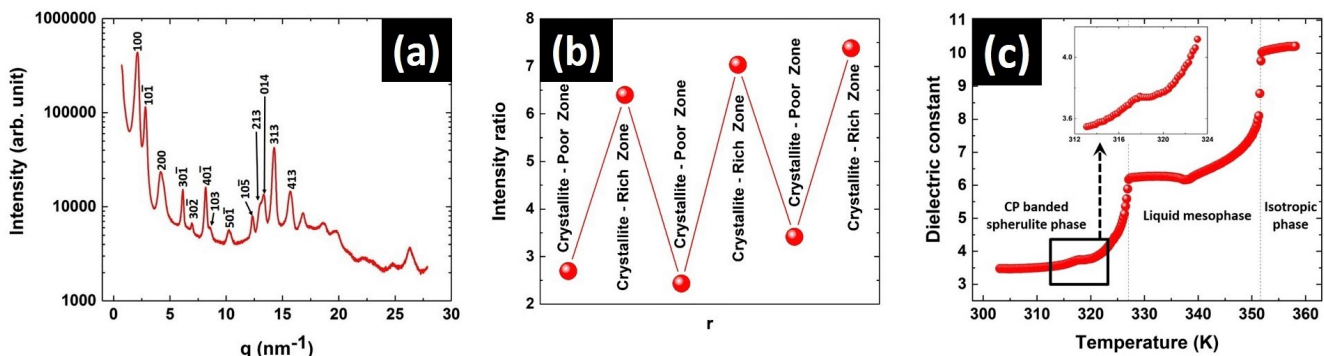


FIG. 3. **Two phase coexistence from XRD, Raman and dielectric profile.** (a) The XRD profile of the banded spherulite of the compound 8OCB. (b) The variation of intensity ratio of the Raman peaks associated with the CN group of the molecules at crystallite-rich and crystallite-poor zones of the banded spherulite along its radial direction. (c) The variation of dielectric constant of the banded spherulite with temperature during heating of the sample. The inset highlights the step change in dielectric constant at 318.1 K.

a broad hump from 11 nm^{-1} to 21 nm^{-1} in this XRD profile. Thus the XRD studies indicate that the banded spherulites of the compound has similar composition as its CP crystal phase.

The spatially resolved variation in the compositions of the sample in the banded spherulitic domain was probed by micro Raman spectroscopy. The stretching vibration peak at 2235 cm^{-1} of the nitrile (CN) bond of 8OCB molecules was used to examine the compositions of the spherulite along its band normal direction. This Raman peak is reported to be quite sensitive to the molecular environment around the CN bond of this molecule [35]. It is asymmetric in the spherulite domain and can be fitted with two closely spaced peaks (see Fig. S4 in the Supplementary Material). The fitted intense peak positioned at 2235 cm^{-1} arises from the nano crystallites of the banded spherulite and less intense shoulder peak positioned at 2226 cm^{-1} originates from the amorphous component

[32]. The ratio of the intensities of these peaks obtained in the crystallite-rich and crystallite-poor zones along the radial direction of the banded spherulite is shown in Fig. 3b. The higher and lower values of this intensity ratio at crystallite-rich and crystallite-poor zones respectively indicates the periodic variation of the compositions along the radial direction of the banded spherulite.

The temperature variation of dielectric constant of the banded spherulite sample during heating it from room temperature is shown in Fig. 3c. A sudden change of slope in the dielectric profile (see inset in Fig. 3c) was observed at 318.1 K indicating a transformation in the sample. But no change in the POM textures of the banded spherulites was found at this temperature. We attribute it to the softening of the amorphous component of the sample. On heating, the bands started to become blur irreversibly at 321.1 K and the texture transformed completely to non-banded spherulite at 325.1 K. The FESEM

studies of this non-banded spherulite revealed that the lengths of the radially aligned fibrillar crystallites were increased and their distribution was uniform along the radial direction giving rise to the non-banded texture (see Fig. S5 in the Supplementary Material). Thus the amorphous component after softening gradually transforms to the crystallites and smectic phase on heating which accounts for the observed increase in dielectric constant with increasing temperature before complete melting of the sample to the smectic phase at 327.6 K [32].

Theoretical Model

In the last few decades, a few theoretical models based on coherent twisting of fibrils have been introduced to account for banded spherulite. The twisting can occur in a system due to multiple causes such as surface stress mismatch [2, 20], isochiral screw dislocation [36, 37], auto deformation [8], self-induced concentration or mechanical fields on growth kinetics [38] and topological defects [39]. In addition some phase field models have also been developed to understand this type of spherulitic growth [40, 41]. However, coherent twisting of the fibrillar crystallites has not been observed in the banded spherulite for this pure liquid crystal compound.

Armed with our experimental results, a time dependent Ginzburg-Landau (TDGL) model C is developed to account for the rhythmic growth of banded spherulitic domain observed in our system. This type of model has been successfully applied in various physical growth phenomena in different systems [42, 43]. Kyu *et al.* simulated ring banded structure using this model and emphasized rhythmic growth assisted banded spherulite formation in polymer blends [44, 45]. The model describes the dynamics of a system using a conserved and a non-conserved order parameters. Our experimental studies have clearly established that the growth of alternating concentric crystallite-rich and crystallite-poor amorphous zones gives rise to the banded spherulites of 8OCB. Therefore, we define the conserved order parameter $\phi = [\rho - \rho_0]/\rho_0$ which describes the local deviation of density in these zones from the average density ρ_0 of the smectic phase. In addition, the non-conserved order parameter $\psi = (\rho_{nc} - \rho_a)/\rho_0$ describes the local composition, where ρ_{nc}/ρ_0 and ρ_a/ρ_0 are the fractional densities of molecules in the nano crystalline and amorphous solid phase respectively. The smectic phase with $\psi = 0$ undergoes a first order transition to the spherulitic domain with $\psi \neq 0$.

Using these order parameters, the free energy density of the system in its smectic phase can be written as

$$f = \frac{A}{2}\phi^2 + \frac{1}{2}k_\phi|\nabla\phi|^2 + W\left[\frac{\alpha(T)}{2}\psi^2 - \frac{1 + \alpha(T)}{3}\psi^3 + \frac{1}{4}\psi^4\right] + \frac{1}{2}k_\psi|\nabla\psi|^2 - \gamma\phi\psi \quad (1)$$

The first two terms in equation 1 represent the free en-

ergy associated with the order parameter ϕ of the sample. We assume that ϕ is non-critical across the transition to the spherulitic state and only the terms upto the quadratic order are retained. The third and fourth terms represent the free energy associated with the order parameter ψ describing the first order phase transition from the smectic phase to the spherulitic state. Here, $0 \leq \alpha(T) = (T - T_c)/(T_m - T_c) \leq 1$ is the temperature dependent parameter driving this first order transition and T_m, T_c are the melting temperature and supercooling limit of the smectic phase respectively. The last term in equation 1 is the lowest order coupling between these order parameters.

Using this free energy expansion, the dimensionless form of the TDGL equations for the system can be written as

$$\frac{\partial\phi}{\partial t} = \nabla^2\left[\phi - \frac{\gamma}{A}\psi - \epsilon\nabla^2\phi\right] \quad (2)$$

$$\epsilon\frac{\partial\psi}{\partial t} = -\frac{\xi_\phi^2}{\lambda_D^2}\left[\psi(\psi - 1)(\psi - \alpha) - \frac{\gamma}{W}\phi - \epsilon\frac{\xi_\psi^2}{\xi_\phi^2}\nabla^2\psi\right] \quad (3)$$

where $\epsilon = (\frac{\gamma^2}{WA} - \alpha)$ is a dimensionless parameter and $\xi_\phi = \sqrt{\frac{k_\phi}{A}}$, $\xi_\psi = \sqrt{\frac{k_\psi}{W}}$ and $\lambda_D = \sqrt{\frac{A\Gamma_\phi}{\Gamma_\psi W}}$ have the dimension of length. Here Γ_ϕ and Γ_ψ are two dynamical coefficients of the system. The detail derivation of these equations is given in the Supplementary Material .

The linear stability analysis (LSA) of equation 2 and equation 3 was performed to investigate the growth of banded spherulite on quenching the system from higher temperature smectic phase. The TDGL equations were linearised with respect to small perturbations $\phi(\vec{r}, t) = \delta\phi_0 e^{\sigma t} e^{i\vec{q}\cdot\vec{r}}$, $\psi(\vec{r}, t) = \delta\psi_0 e^{\sigma t} e^{i\vec{q}\cdot\vec{r}}$ about the smectic phase ($\phi = 0, \psi = 0$). The resulting eigenvalue equations (see Supplementary Material) determine the stability of the smectic phase with respect to these perturbative modes for different values of the control parameter α . The modes with negative real part of σ decay to zero and are therefore stable while the modes with positive real part of σ grow with time and are unstable.

Fig. 4a shows the variation of σ with the wave vector q for different values of α . As can be seen from Fig. 4a, σ is positive for modes with wave vector q lying between zero and q_{max} and these unstable modes give rise to the formation of banded spherulite in this system. Among these unstable modes, σ has the highest positive value for $q = q_c$ and this most unstable mode will be dominant during the growth of the banded spherulite. Fig. 4b shows the variation of q_{max} and q_c with the parameter α obtained from LSA. Though q_c varies strongly with α , the q_{max} does not vary appreciably with it. The wavelength corresponding to this dominant mode calculated from the LSA is compared with the experimentally measured band spacing of the banded spherulite as shown in Fig. 4c for different values of supercooling. The theoretical result agrees well with the experimental data confirming the general validity of this model.

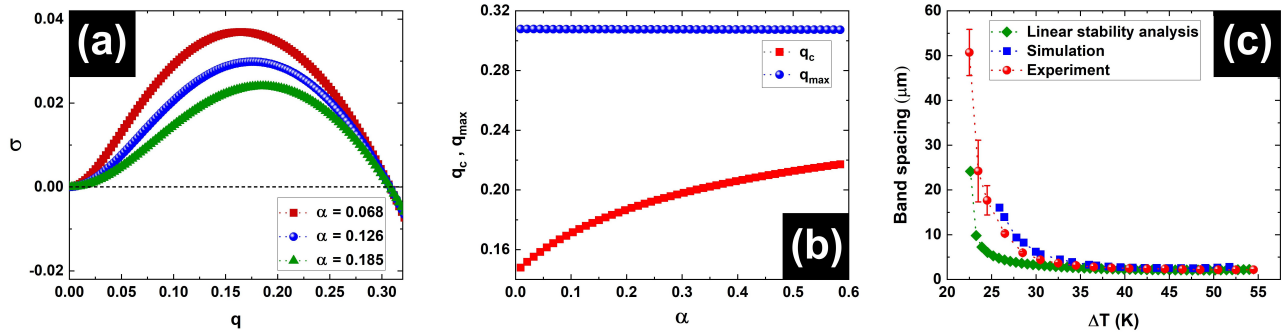


FIG. 4. **Effect of supercooling on banded spherulite.** (a) The variation of σ with the wave vector q for different values of α . The modes in the wave vector range $0 < q < q_{max}$ are unstable. (b) The variation of q_{max} and q_c as a function of α . (c) Comparison between experimental, linear stability analysis and simulation results for the variation of band spacing with supercooling ΔT . The values of the parameters used for the theoretical model are $\gamma/A = 0.242$, $W/A = 0.1$, $\xi_\phi = 0.04 \mu\text{m}$, $\xi_\psi = 3.16\xi_\phi$, $\lambda_D = 1.41\xi_\phi$.

A general analytical method of finding solutions of the coupled nonlinear TDGL equations given by equations 2 and 3 is not known. These equations were solved numerically under no flux boundary condition using a finite difference method in two dimension. The numerical solutions of the order parameters ϕ and ψ for a banded spherulite growing from a seed at the centre are shown in Fig. 5a and Fig. 5b respectively (also see Fig. S6 in the Supplementary Material). The formation of the ring banded structure is clearly observed as found experimentally. Fig. 5c shows the graphical profiles of the order parameters along a radial direction of the spherulite. The order parameters vary periodically and in phase along the radial direction during the growth of the spherulite. This in phase variation of the order parameters arises due to their bilinear coupling with $\gamma > 0$ in equation 1.

In these numerical computations, a banded spherulite grows from an initial nano crystallite seed on sufficient supercooling of the smectic phase. The nano crystallites have higher density compared to the amorphous state. Thus the growth of this nano crystallite-rich domain leads to decrease in density around it due to the depletion of the molecules. When the density decreases sufficiently, it promotes the formation of a crystallite-poor amorphous domain around the initial crystallite-rich domain. The growth of this crystallite-poor band in turn increases the density around its periphery and leads to the nucleation of another nano crystallite-rich band. The growth continues with the formation of alternating crystallite-rich and crystallite-poor bands in a periodic manner along the radial direction of the spherulite as in-

dicated in Fig. 5. The radius of the numerically simulated banded spherulite grows with time in a rhythmic fashion as shown in the Supplementary Material Fig. S7.

The spacing between two successive bands of the spherulite was also calculated from the numerical results for different values of supercooling ΔT . The numerically computed band spacing as a function of supercooling agrees very well with the experimental data as shown in Fig. 4c. This figure also shows that the experimentally measured band spacing of the spherulite tends to diverge on approaching $\Delta T \sim 22.5$ K from above. Below this supercooling, only the formation of non-banded spherulites was observed experimentally. Both the LSA and numerical results account for this divergence of band spacing. This divergence arises from a singularity of the TDGL equations for the parameter ϵ in equations 2 and 3 being zero. Therefore, the order parameter ψ is determined by the equation $\psi(\psi - 1)(\psi - \alpha) = \frac{\gamma}{W}\phi$ and only the order parameter ϕ controls the dynamics of the system. A comparison between the computed and experimentally measured growth velocities of banded spherulite gives the translational diffusion constant ($A\Gamma_\phi$) of the molecules as $10^{-11} \text{ m}^2/\text{sec}$ which agrees with the earlier reported data on 8OCB [46]. The consistency of the numerical results was also checked on solving the TDGL equations using the finite element method (FEniCS python package)(see Fig. S8 in the Supplementary Material). However, the numerical solutions of these nonlinear equations show that the ring banded pattern under certain conditions becomes unstable leading to the breaking of the spherical symmetry of the growth pattern. The detail on these numerical results will be published elsewhere.

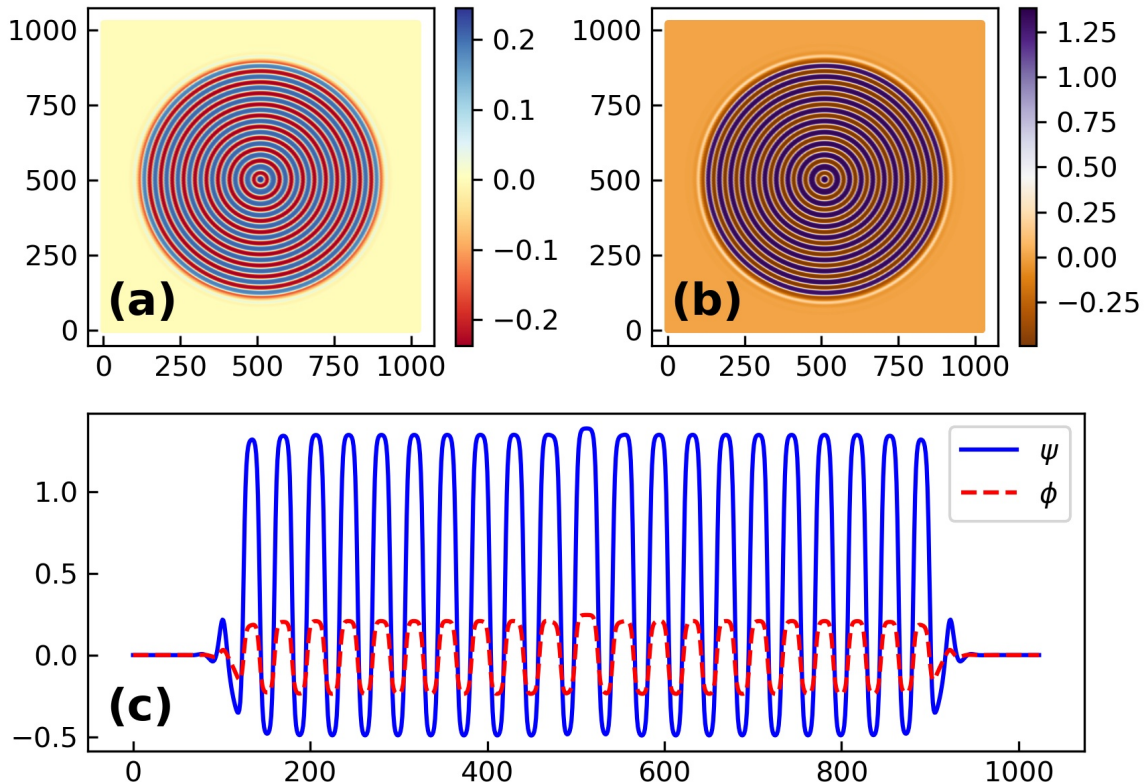


FIG. 5. **Simulated banded spherulite domain.** The colour coded representation of the order parameters (a) ϕ and (b) ψ of a banded spherulite obtained from the numerical solution of the TDGL equations at $\Delta T = 39.5$ K. The model parameters used are $\gamma/A = 0.242$, $W/A = 0.1$, $\zeta_\phi = 0.04 \mu\text{m}$, $\zeta_\psi = 3.16\zeta_\phi$, $\lambda_D = 1.41\zeta_\phi$, time step size $dt = 0.01$ and spatial step size $dx = dy = 1.0$. (c) The graphical profiles of ϕ and ψ along a radial axis of the simulated banded spherulite.

IV. SUMMARY

We have studied the banded spherulitic growth of the solid phase of a pure liquid crystalline compound from its melt. The compound exhibits coexistence of fibrillar nano crystallites and an amorphous phase in its most stable solid state at room temperature. The banded spherulites are formed due to the rhythmic generation of crystallite-rich and crystallite-poor amorphous concentric zones on supercooling the smectic phase of the compound. This produces the modulation in birefringence

which gives rise to the interference colour bands observed between crossed polarisers. A theoretical model using the time dependent Ginzburg-Landau theory is developed to account for the observed banded spherulitic growth in this compound which agrees well with the experimental observations.

ACKNOWLEDGMENTS

We thank Ms Vashudha K. N. for her help in acquiring XRD data and K. M. Yatheendran for his help in FESEM and confocal imaging.

- [1] B. Crist and J. M. Schultz, *Progress in Polymer Science* **56**, 1 (2016).
 [2] B. Lotz and S. Z. Cheng, *Polymer* **46**, 577 (2005).

- [3] G. Lofgren, *American Journal of Science* **274**, 243 (1974), <https://www.ajsonline.org/content/274/3/243.full.pdf>.
 [4] R. Coish and L. A. Taylor, *Earth and Planetary Science Letters* **42**, 389 (1979).

- [5] R. J. Kirkpatrick, *American Journal of Science* **274**, 215 (1974), <https://www.ajsonline.org/content/274/3/215.full.pdf>.
- [6] I. Minkoff and W. C. Nixon, *Journal of Applied Physics* **37**, 4848 (1966), <https://doi.org/10.1063/1.1708149>.
- [7] J. Bisault, G. Ryschenkow, and G. Faivre, *Journal of Crystal Growth* **110**, 889 (1991).
- [8] A. G. Shtukenberg, Y. O. Punin, E. Gunn, and B. Kahr, *Chemical Reviews* **112**, 1805 (2012), pMID: 22103741, <https://doi.org/10.1021/cr200297f>.
- [9] R. Beck and J.-P. Andreassen, *Crystal Growth & Design* **10**, 2934 (2010), <https://doi.org/10.1021/cg901460g>.
- [10] Y. Oaki and H. Imai, *Journal of the American Chemical Society* **126**, 9271 (2004), pMID: 15281817, <https://doi.org/10.1021/ja048661+>.
- [11] A. Thomas, E. Rosseeva, O. Hochrein, W. Carrillo-Cabrera, P. Simon, P. Duchstein, D. Zahn, and R. Kniep, *Chemistry – A European Journal* **18**, 4000 (2012), <https://chemistry-europe.onlinelibrary.wiley.com/doi/pdf/10.1002/chem.201102228>.
- [12] C.-Y. Sun, M. A. Marcus, M. J. Frazier, A. J. Giuffre, T. Mass, and P. U. P. A. Gilbert, *ACS Nano* **11**, 6612 (2017), pMID: 28564539, <https://doi.org/10.1021/acsnano.7b00127>.
- [13] U. Al-Atar, A. A. Bokov, D. Marshall, J. M. H. Teichman, B. D. Gates, Z.-G. Ye, and N. R. Branda, *Chemistry of Materials* **22**, 1318 (2010), <https://doi.org/10.1021/cm901751g>.
- [14] P. S. Chow, X. Y. Liu, J. Zhang, and R. B. H. Tan, *Applied Physics Letters* **81**, 1975 (2002), <https://doi.org/10.1063/1.1506208>.
- [15] J. E. Coleman, B. J. Allan, and B. L. Vallee, *Science* **131**, 350 (1960), <https://www.science.org/doi/pdf/10.1126/science.131.3397.350>.
- [16] M. R. H. Krebs, C. E. MacPhee, A. F. Miller, I. E. Dunlop, C. M. Dobson, and A. M. Donald, *Proceedings of the National Academy of Sciences* **101**, 14420 (2004), <https://www.pnas.org/content/101/40/14420.full.pdf>.
- [17] F. Catalina and L. Cifuentes, *Science* **169**, 183 (1970), <https://www.science.org/doi/pdf/10.1126/science.169.3941.183>.
- [18] D. Brewster, *Transactions of the Royal Society of Edinburgh* **20**, 607–623 (1853).
- [19] H. D. Keith and F. J. Padden, *Journal of Applied Physics* **34**, 2409 (1963), <https://doi.org/10.1063/1.1702757>.
- [20] H. Keith and F. Padden, *Polymer* **25**, 28 (1984).
- [21] A. G. Shtukenberg, J. Freudenthal, and B. Kahr, *Journal of the American Chemical Society* **132**, 9341 (2010), pMID: 20405919, <https://doi.org/10.1021/ja101491n>.
- [22] A. G. Shtukenberg, X. Cui, J. Freudenthal, E. Gunn, E. Camp, and B. Kahr, *Journal of the American Chemical Society* **134**, 6354 (2012), pMID: 22413815, <https://doi.org/10.1021/ja300257m>.
- [23] W. Pisula, M. Kastler, D. Wasserfallen, T. Pakula, and K. Müllen, *Journal of the American Chemical Society* **126**, 8074 (2004), pMID: 15225022, <https://doi.org/10.1021/ja048351r>.
- [24] X. Cui, A. L. Rohl, A. Shtukenberg, and B. Kahr, *Journal of the American Chemical Society* **135**, 3395 (2013), pMID: 23425247, <https://doi.org/10.1021/ja400833r>.
- [25] A. Shtukenberg, J. Freudenthal, E. Gunn, L. Yu, and B. Kahr, *Crystal Growth & Design* **11**, 4458 (2011), <https://doi.org/10.1021/cg200640g>.
- [26] T.-F. Lin, R.-M. Ho, C.-H. Sung, and C.-S. Hsu, *Chemistry of Materials* **18**, 5510 (2006), <https://doi.org/10.1021/cm061666g>.
- [27] J. L. Hutter and J. Bechhoefer, *Phys. Rev. Lett.* **79**, 4022 (1997).
- [28] J. L. Hutter and J. Bechhoefer, *Journal of Crystal Growth* **217**, 332 (2000).
- [29] C. Wang, R. Thomann, J. Kressler, Y. Thomann, K. Crämer, B. Stühn, P. Svoboda, and T. Inoue, *Acta Polymerica* **48**, 354 (1997).
- [30] J. Chen and D. Yang, *Macromolecules* **38**, 3371 (2005), <https://doi.org/10.1021/ma047904f>.
- [31] J. Chen and D. Yang, *Journal of Polymer Science Part B: Polymer Physics* **45**, 3011 (2007), <https://onlinelibrary.wiley.com/doi/pdf/10.1002/polb.21124>.
- [32] S. Ghosh and A. Roy, *RSC Adv.* **11**, 4958 (2021).
- [33] A. Shtukenberg, E. Gunn, M. Gazzano, J. Freudenthal, E. Camp, R. Sours, E. Rosseeva, and B. Kahr, *ChemPhysChem* **12**, 1558 (2011), <https://chemistry-europe.onlinelibrary.wiley.com/doi/pdf/10.1002/cphc.201000963>.
- [34] E. M. Woo, G. Lugito, and C.-E. Yang, *CrystEngComm* **18**, 977 (2016).
- [35] K. Hori, M. Kuribayashi, and M. Iimuro, *Phys. Chem. Chem. Phys.* **2**, 2863 (2000).
- [36] D. Patel and D. Bassett, *Polymer* **43**, 3795 (2002).
- [37] A. Toda, T. Arita, and M. Hikosaka, *Polymer* **42**, 2223 (2001).
- [38] J. M. Schultz, *Polymer* **44**, 433 (2003).
- [39] Y. Hatwalne and M. Muthukumar, *Phys. Rev. Lett.* **105**, 107801 (2010).
- [40] L. Gránásy, T. Pusztai, G. Tegze, J. A. Warren, and J. F. Douglas, *Phys. Rev. E* **72**, 011605 (2005).
- [41] A. Fang and M. Haataja, *Phys. Rev. E* **92**, 042404 (2015).
- [42] A. A. Wheeler, W. J. Boettinger, and G. B. McFadden, *Phys. Rev. A* **45**, 7424 (1992).
- [43] K. R. Elder, F. Drolet, J. M. Kosterlitz, and M. Grant, *Phys. Rev. Lett.* **72**, 677 (1994).
- [44] T. Kyu, H.-W. Chiu, A. J. Guenther, Y. Okabe, H. Saito, and T. Inoue, *Phys. Rev. Lett.* **83**, 2749 (1999).
- [45] H. Xu, H.-W. Chiu, Y. Okabe, and T. Kyu, *Phys. Rev. E* **74**, 011801 (2006).
- [46] S. V. Dvinskikh and I. Furó, *Phys. Rev. E* **86**, 031704 (2012).

Observation of banded spherulite in a pure compound by rhythmic growth

Subhadip Ghosh, Dipak Patra and Arun Roy

Soft-Condensed Matter Group, Raman Research Institute, Bangalore 560080, India

March 18, 2022

Supplementary Material

Sample preparation for Cryo-SEM imaging

For cryo-SEM imaging, a small brass container was filled with the sample above its clearing temperature using a hot stage. After that it was dipped in liquid nitrogen for fast cooling which produced the banded spherulites. It was then transferred to the cryo-sample preparation chamber (Quorum Technologies PP3000T) of the FESEM system maintained at a temperature of 103 K. The sample was then heated to 183 K to make it soft and the upper portion of the sample was scraped off for removing the ice content. The newly opened sample surface was then sputter coated with platinum and transferred to the main unit for SEM imaging where the sample was maintained at 83 K.

Theoretical Discussions

We provide here the details of the linear stability analysis and numerical methods for the solution of the time dependent Ginzburg-Landau model C equations of the banded spherulitic growth in our sample. In the main text, two order parameters are defined to describe the banded spherulitic growth. The conserved order parameter $\phi = [\rho - \rho_0]/\rho_0$ describes the local deviation of density from the average density ρ_0 in the smectic phase and the non-conserved order parameter $\psi = (\rho_{nc} - \rho_a)/\rho_0$ describes the local composition. The parameters ρ_{nc}/ρ_0 and ρ_a/ρ_0 are the fractional density of molecules in the nano crystallite and the amorphous solid phase respectively. The free energy density of the system in terms of these order parameters can be written as

$$f = \frac{A}{2}\phi^2 + \frac{1}{2}k_\phi|\nabla\phi|^2 + W\left[\frac{\alpha(T)}{2}\psi^2 - \frac{1+\alpha(T)}{3}\psi^3 + \frac{1}{4}\psi^4\right] + \frac{1}{2}k_\psi|\nabla\psi|^2 - \gamma\phi\psi. \quad (1)$$

The temperature dependent parameter α assumed as $0 \leq \alpha(T) \leq 1$ drives to the first order transition in the system. For simplicity, all other coefficients of the expansion are assumed to be temperature independent constants in our model. The time dependent Ginzburg-Landau (TDGL) Model C equations for the order parameters are given by

$$\begin{aligned} \frac{\partial\phi}{\partial t} &= \Gamma_\phi \nabla^2 \frac{\delta F}{\delta\phi}, \\ \frac{\partial\psi}{\partial t} &= -\Gamma_\psi \frac{\delta F}{\delta\psi}, \end{aligned}$$

where right hand side of these equations is obtained by taking the variational derivative of the free energy F with respect to the order parameters.

Using the free energy density in eq. 1, the dynamical equations for the order parameters become

$$\frac{\partial\phi}{\partial t} = \Gamma_\phi \nabla^2 \left[A\phi - \gamma\psi - k_\phi \nabla^2 \phi \right]$$

$$\frac{\partial \psi}{\partial t} = -\Gamma_\psi \left[W\psi(\psi - 1)(\psi - \alpha) - \gamma\phi - k_\psi \nabla^2 \psi \right].$$

The above equations can be made dimensionless by the transformations $x \rightarrow x' = \frac{\sqrt{\epsilon}}{\xi_\phi} x$, $t \rightarrow t' = \frac{\epsilon \Gamma_\phi A}{\xi_\phi^2} t$. The dimensionless form of these equations after omitting for convenience the prime notation on the variables becomes

$$\frac{\partial \phi}{\partial t} = \nabla^2 \left[\phi - \frac{\gamma}{A} \psi - \epsilon \nabla^2 \phi \right] \quad (2)$$

$$\frac{\partial \psi}{\partial t} = -\frac{\xi_\phi^2}{\epsilon \lambda_D^2} \left[\psi(\psi - 1)(\psi - \alpha) - \frac{\gamma}{W} \phi - \epsilon \frac{\xi_\psi^2}{\xi_\phi^2} \nabla^2 \psi \right], \quad (3)$$

where the parameters are $\epsilon = \frac{\gamma^2}{WA} - \alpha$, $\xi_\phi = \sqrt{\frac{k_\phi}{A}}$, $\xi_\psi = \sqrt{\frac{k_\psi}{W}}$ and $\lambda_D^2 = \frac{A\Gamma_\phi}{\Gamma_\psi W}$. As usual in Landau theory, the parameter α is assumed to be linearly dependent on temperature as $\alpha = \delta(T - T_c)$. The melting temperature of 8OCB is 327.6 K and smectic phase is absolutely stable above this temperature. Hence, we have considered that α takes the maximum value 1 at this temperature $T_m = 327.6$ K. We have assumed the temperature $T_c = 273.1$ K denoting the lower limit of stability of the smectic phase which is difficult to find experimentally due to large range of supercooling of the smectic phase. Then the parameter $\alpha(T) = (T - T_c)/(T_m - T_c)$.

Linear Stability Analysis

The linear stability analysis (LSA) was performed to investigate the growth of banded spherulite on quenching the system from higher temperature smectic phase. The TDGL equations were linearised with respect to small perturbations about the fixed point ($\phi^* = 0$, $\psi^* = 0$). Hence, we get the following linear dynamical equations by considering $\phi(\vec{r}, t) = \phi^* + \delta\phi(\vec{r}, t)$ and $\psi(\vec{r}, t) = \psi^* + \delta\psi(\vec{r}, t)$.

$$\begin{aligned} \frac{\partial \delta\phi}{\partial t} &= \nabla^2 \left[\delta\phi - \frac{\gamma}{A} \delta\psi - \epsilon \nabla^2 \delta\phi \right] \\ \frac{\partial \delta\psi}{\partial t} &= -\frac{\xi_\phi^2}{\epsilon \lambda_D^2} \left[g(\psi^*) - \frac{\gamma}{W} \phi^* \right] - \frac{\xi_\phi^2}{\epsilon \lambda_D^2} \left[g'(\psi^*) \delta\psi - \frac{\gamma}{W} \delta\phi - \epsilon \frac{\xi_\psi^2}{\xi_\phi^2} \nabla^2 \delta\psi \right] \end{aligned}$$

where $g(\psi) = \psi(\psi - 1)(\psi - \alpha)$ and $g'(\psi)$ is the derivative of $g(\psi)$ with respect to ψ . In our model $g(0) = 0$ and $g'(0) = \alpha > 0$. Assuming the solution of the above two equations in the form $\delta\phi = \delta\phi_0 e^{\sigma t} e^{i\vec{q}\cdot\vec{r}}$ and $\delta\psi = \delta\psi_0 e^{\sigma t} e^{i\vec{q}\cdot\vec{r}}$, we obtain

$$\begin{aligned} \sigma \delta\phi_0 e^{\sigma t} e^{i\vec{q}\cdot\vec{r}} &= \left[-(q^2 + \epsilon q^4) \delta\phi_0 + \frac{\gamma}{A} q^2 \delta\psi_0 \right] e^{\sigma t} e^{i\vec{q}\cdot\vec{r}} \\ \sigma \delta\psi_0 e^{\sigma t} e^{i\vec{q}\cdot\vec{r}} &= -\frac{\xi_\phi^2}{\epsilon \lambda_D^2} \left[\alpha \delta\psi_0 - \frac{\gamma}{W} \delta\phi_0 + \epsilon \frac{\xi_\psi^2}{\xi_\phi^2} q^2 \delta\psi_0 \right] e^{\sigma t} e^{i\vec{q}\cdot\vec{r}} \end{aligned}$$

or

$$\begin{aligned} \sigma \delta\phi_0 &= -(\epsilon q^4 + q^2) \delta\phi_0 + \frac{\gamma}{A} q^2 \delta\psi_0 \\ \sigma \delta\psi_0 &= \frac{\xi_\phi^2}{\epsilon \lambda_D^2} \frac{\gamma}{W} \delta\phi_0 - \frac{\xi_\phi^2}{\epsilon \lambda_D^2} \left[\alpha + \epsilon \frac{\xi_\psi^2}{\xi_\phi^2} q^2 \right] \delta\psi_0 \end{aligned}$$

These equations can be written as the eigenvalue equation $B \begin{pmatrix} \delta\phi_0 \\ \delta\psi_0 \end{pmatrix} = \sigma \begin{pmatrix} \delta\phi_0 \\ \delta\psi_0 \end{pmatrix}$, where

$$B = \begin{bmatrix} -(q^2 + \epsilon q^4) & \frac{\gamma}{A} q^2 \\ \frac{\gamma \xi_\phi^2}{\epsilon W \lambda_D^2} & -\frac{\xi_\phi^2}{\epsilon \lambda_D^2} \left[\alpha + \epsilon \frac{\xi_\psi^2}{\xi_\phi^2} q^2 \right] \end{bmatrix}.$$

The eigenvalues of the matrix B can be found from the equation $\sigma^2 - \tau\sigma + \Delta = 0$, where $\tau = Tr(B)$ and $\Delta = det(B)$ are given by

$$\begin{aligned}\tau &= -\left[(q^2 + \epsilon q^4) + \frac{\xi_\phi^2}{\epsilon\lambda_D^2}\left[\alpha + \epsilon\frac{\xi_\psi^2}{\xi_\phi^2}q^2\right]\right] \\ \Delta &= \frac{\xi_\phi^2}{\epsilon\lambda_D^2}(q^2 + \epsilon q^4)\left[\alpha + \epsilon\frac{\xi_\psi^2}{\xi_\phi^2}q^2\right] - \frac{\gamma^2\xi_\phi^2}{\epsilon WA\lambda_D^2}q^2.\end{aligned}$$

The eigenvalues $\sigma_\pm = \frac{\tau \pm \sqrt{\tau^2 - 4\Delta}}{2}$ can be complex in general. If the real part of any of these eigenvalues is positive, the corresponding mode grows with time ($\sim e^{\sigma t}$) and the fixed point is unstable. On the other hand, the fixed point is stable if the real part of both the eigenvalues is negative. The real part of σ_- is negative for all values of q as $\tau < 0$. But the real part of σ_+ can be positive if $\Delta < 0$ giving rise to the unstable modes. The Δ becomes negative in the range $0 < q < q_{max}$ where the limits of the range can be obtained from the equation $\Delta(q) = 0$ or

$$\frac{\xi_\phi^2}{\lambda_D^2}\left[\epsilon\frac{\xi_\psi^2}{\xi_\phi^2}q^6 + \left(\alpha + \frac{\xi_\psi^2}{\xi_\phi^2}\right)q^4 - q^2\right] = 0$$

giving the lower root $q = 0$ and the upper real root

$$q_{max} = \frac{1}{\sqrt{2\epsilon}}\left[\sqrt{\frac{4\epsilon\xi_\phi^2}{\xi_\psi^2} + \left(1 + \frac{\alpha\xi_\phi^2}{\xi_\psi^2}\right)^2} - \left(1 + \frac{\alpha\xi_\phi^2}{\xi_\psi^2}\right)\right]^{1/2}.$$

The fastest growing mode $q = q_c$ can be found by maximising σ_+ with respect to q . The wavelength of this dominant growing mode determined numerically is compared with the experimentally observed band spacing of the system for different values of supercooling. The theoretically calculated band spacing diverges on approaching the supercooling $\Delta T = 22.5$ K as observed experimentally in our system. This divergence can be attributed to the singularity of the TDGL equations at $\epsilon = 0$ in our model.

Simulation

For numerical solutions, we constructed three lower order partial differential equations from the higher order the TDGL equations by considering an additional dynamical variable μ as

$$\frac{\partial\phi}{\partial t} = \nabla^2\mu \tag{4}$$

$$\mu = \phi - \frac{\gamma}{A}\psi - \epsilon\nabla^2\phi \tag{5}$$

$$\frac{\partial\psi}{\partial t} = -\frac{\xi_\phi^2}{\epsilon\lambda_D^2}\left[\psi(\psi - 1)(\psi - \alpha) - \frac{\gamma}{W}\phi - \epsilon\frac{\xi_\psi^2}{\xi_\phi^2}\nabla^2\psi\right] \tag{6}$$

These equations were solved numerically for two dimensional system under the no flux boundary conditions i.e., $\vec{\nabla}\phi \cdot \hat{n}|_{\partial\Omega} = 0$, $\vec{\nabla}\mu \cdot \hat{n}|_{\partial\Omega} = 0$ and $\vec{\nabla}\psi \cdot \hat{n}|_{\partial\Omega} = 0$, where $\partial\Omega$ denotes the boundary. Initially ϕ was set to zero at all points in the simulation domain and ψ was set to a nonzero value for a small seed at the centre of the simulation domain which was assumed to be a square lattice. We used the finite difference method for both space and time for the discretization of these equations. Five points were used for discretization of the Laplacian operator. We performed the finite difference simulation for the parameter set ($W/A = 0.1$, $\gamma/A = 0.2423$, $\xi_\phi = 0.04 \mu\text{m}$, $\xi_\psi = 3.16\xi_\phi$, $\xi_\phi^2/\lambda_D^2 = 5W/A$) obtained from the linear stability analysis. Some numerically obtained ring banded patterns for different values of α are shown in Figure S6. The band spacing in the pattern was determined using ImageJ tools. We have compared the numerically obtained band spacing data with the experimental as well as the linear stability analysis data in the main article.

The radius of the numerically simulated banded spherulite grows with time in a rhythmic fashion. The staircase type growth of dimensionless radius R with dimensionless time is shown in (Figure S7).

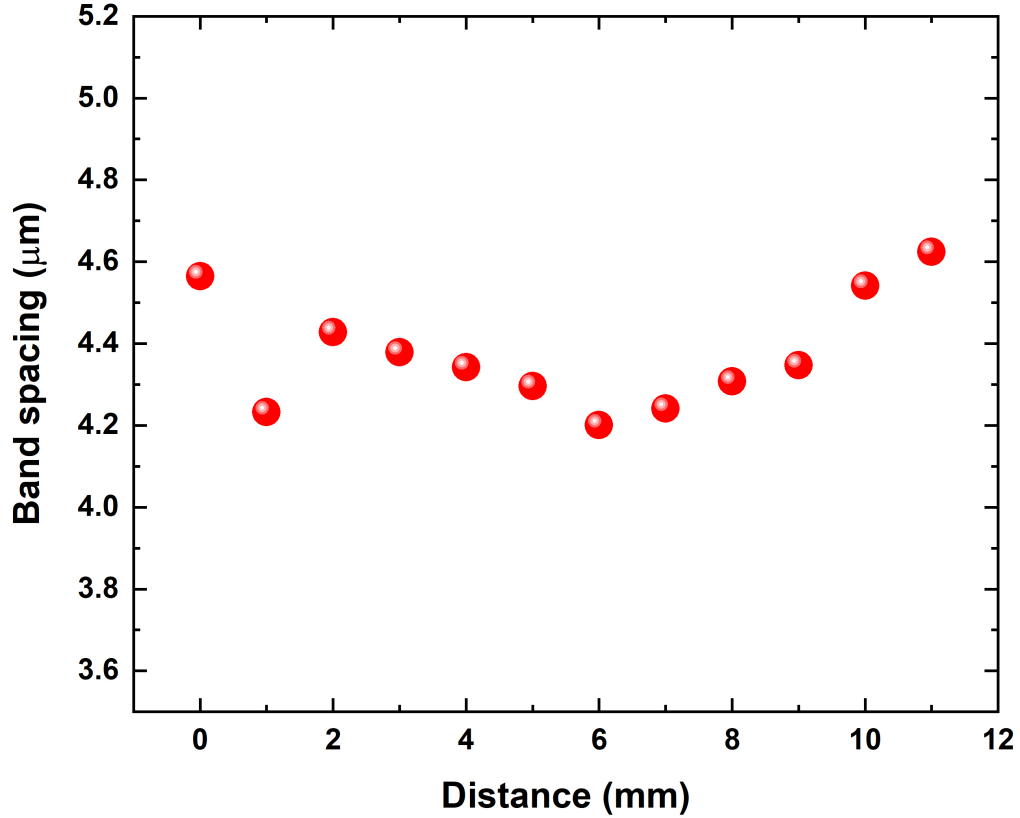


Figure S1: **Band spacing with sample thickness.** The variation of band spacing of a banded spherulite of 8OCB along the length of a wedge type cell with increasing sample thickness. The thickness of the sample increases by six times over 11 mm length of the wedge cell but the band spacing of the spherulite remains same within experimental error. Thus band spacing is not determined by the thickness of the sample as also found in our theoretical model.

Each step represents the duration of a full band growth. Though this growth is nonlinear at each individual step, it shows on average a linear growth law with time. The growth velocity of the ring banded pattern can be found from this linear relationship. It was not possible to resolve experimentally the rhythmic growth pattern due to relatively fast growth of the banded spherulite in our sample.

The TDGL equations were also solved numerically using finite element method (FEM) for some parameter values. We implemented the above equations (eq. 4) in the finite element open source software FEniCS and solved these equations on a 257×257 square mesh. The FEM computations show ring banded patterns (Figure S8) similar to finite difference results (Figure S6). The FEM computations are found to be slow compared to the finite difference method and all the results reported in this paper were performed in the finite difference method.

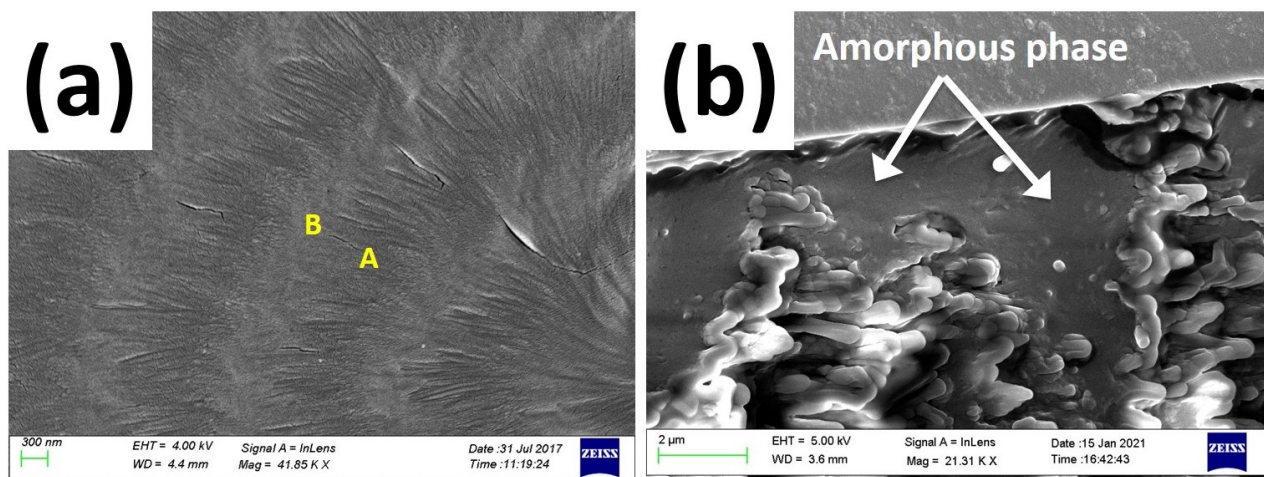


Figure S2: **Two phase coexistence in banded spherulite.** (a) The cryo-SEM image of 8OCB banded spherulite formed after quenching the sample from its melt in liquid nitrogen. Crystallite-rich and crystallite-poor zones are marked as **A** and **B** respectively. (b) The SEM texture of the cross-sectional plane of the banded spherulite obtained by cutting it into two halves. The spherulite was formed on a cleaned coverslip on cooling the sample to room temperature. The amorphous domains in addition to the nano crystallites are clearly visible.

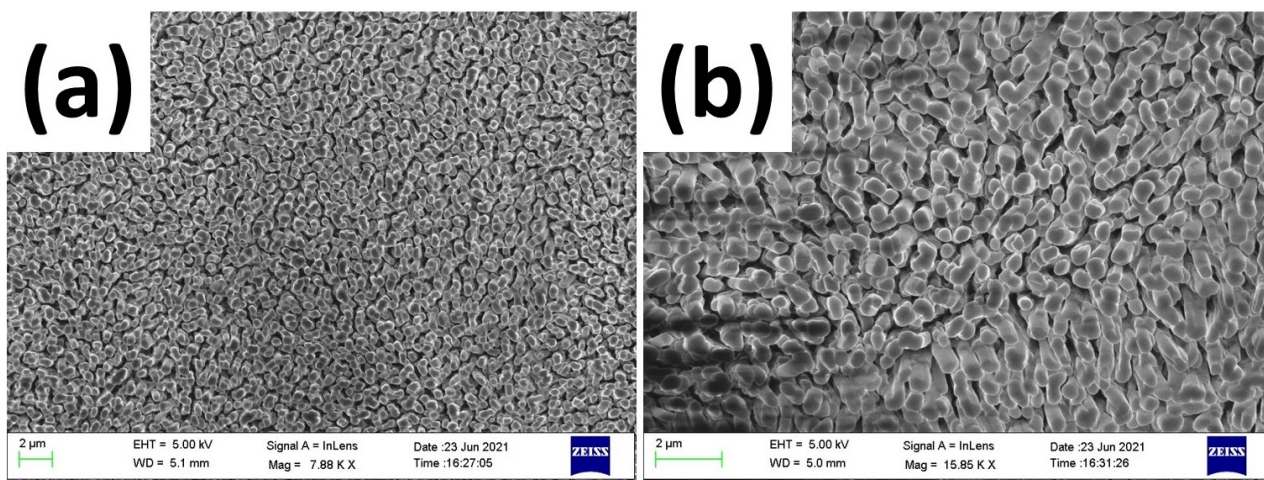


Figure S3: **Cross sectional image of nano crystallites.** (a) The SEM texture of the cleaved surface of the banded spherulite showing the cross sectional view of the fibrillar nano crystallites of 8OCB. The spherulite was formed on a coverslip by cooling the sample from its melt to room temperature and then cut in the middle for the cross sectional view of the banded spherulite domain. (b) The same texture with higher magnification.

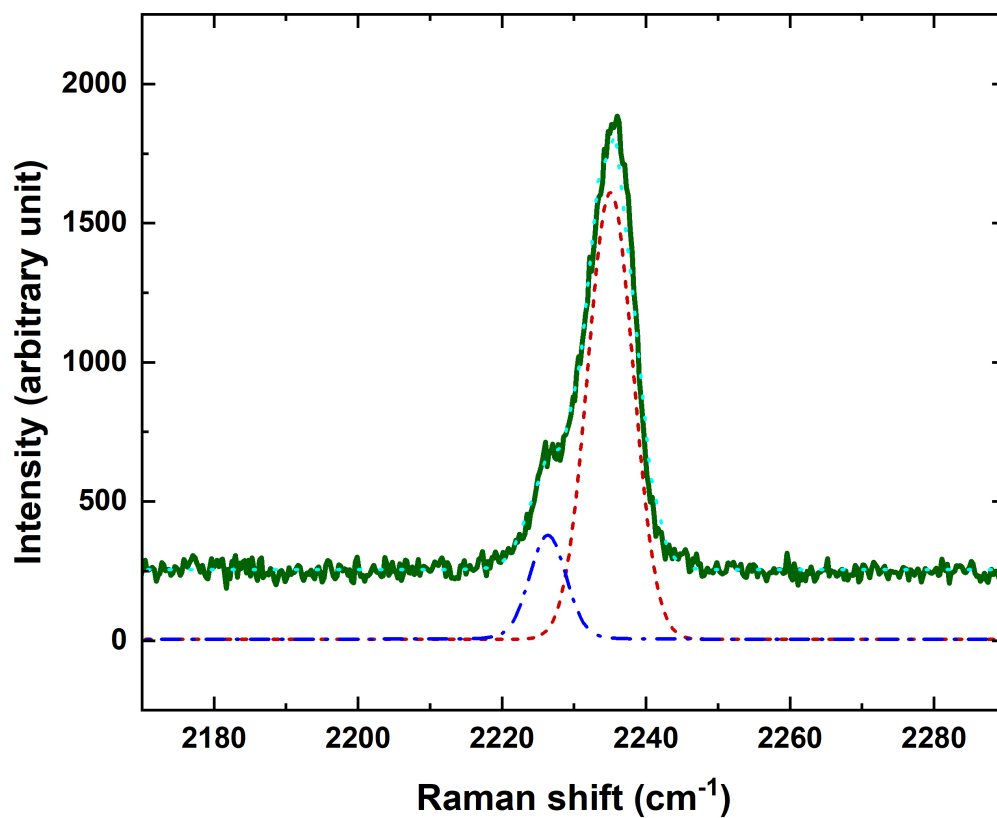


Figure S4: **CN peak from banded spherulite.** The asymmetric Raman peak profile (green line) for the CN stretching vibration of 8OCB in the banded spherulite domain. This peak profile can be fitted with two closely positioned peaks at 2226 cm⁻¹ (blue dash dot line) and 2235 cm⁻¹ (red dash line) respectively. These two peaks for CN stretching vibration arise from the amorphous and nano crystallite components of the banded spherulite respectively.

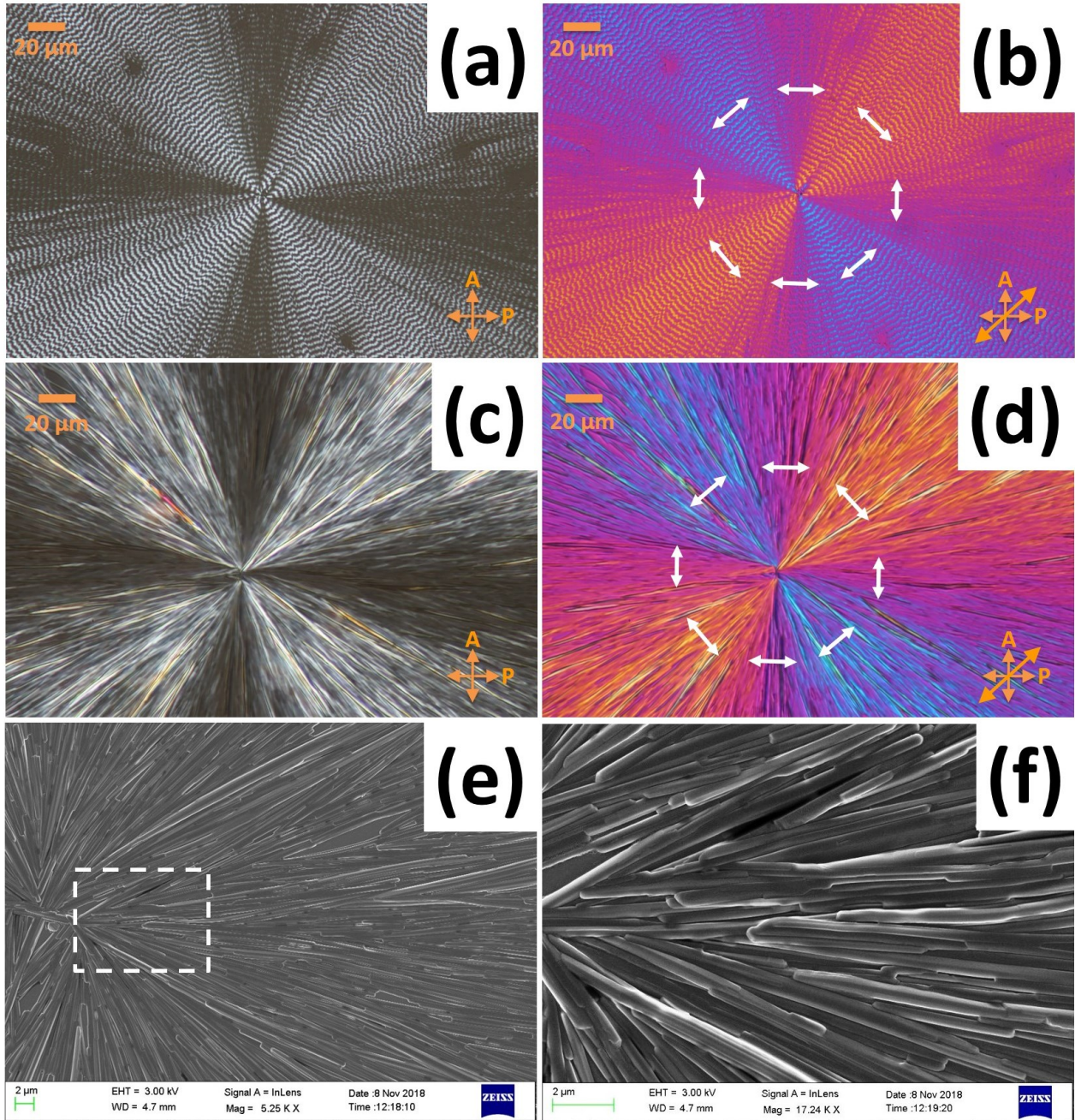


Figure S5: **Transformation of banded spherulite on heating.** The polarised optical microscope (POM) images of a banded spherulite of 8OCB at room temperature (a) between crossed polarisers and (b) with a λ -plate inserted in the optical path in addition to the crossed polarisers. The interference colours indicate that the spherulite is optically negative. The direction of major refractive index in the sample plane is denoted by white double headed arrows around the seed. (c) The POM texture after holding the banded spherulite at 325.1 K for 1 hour followed by cooling it to room temperature. Banded spherulite changes irreversibly to a non-banded one. Dark arms of the Maltese cross parallel to the polarisers remain invariant on rotation of the sample between crossed polarisers. (d) The same texture as shown in (c) after inserting a λ -plate in the optical path. The interference colours indicate that the non-banded spherulite remains optically negative with the major refractive index along the white double headed arrows around the seed. (e) The FESEM image of the same sample as in (c) showing the radially aligned fibrillar nano crystallites with no periodic variation of their density. The crystalline fibrils become longer on transformation of the banded spherulite to the non-banded one. (f) The magnified view of the selected portion in (e) depicting no twist in the nano crystalline fibrils.

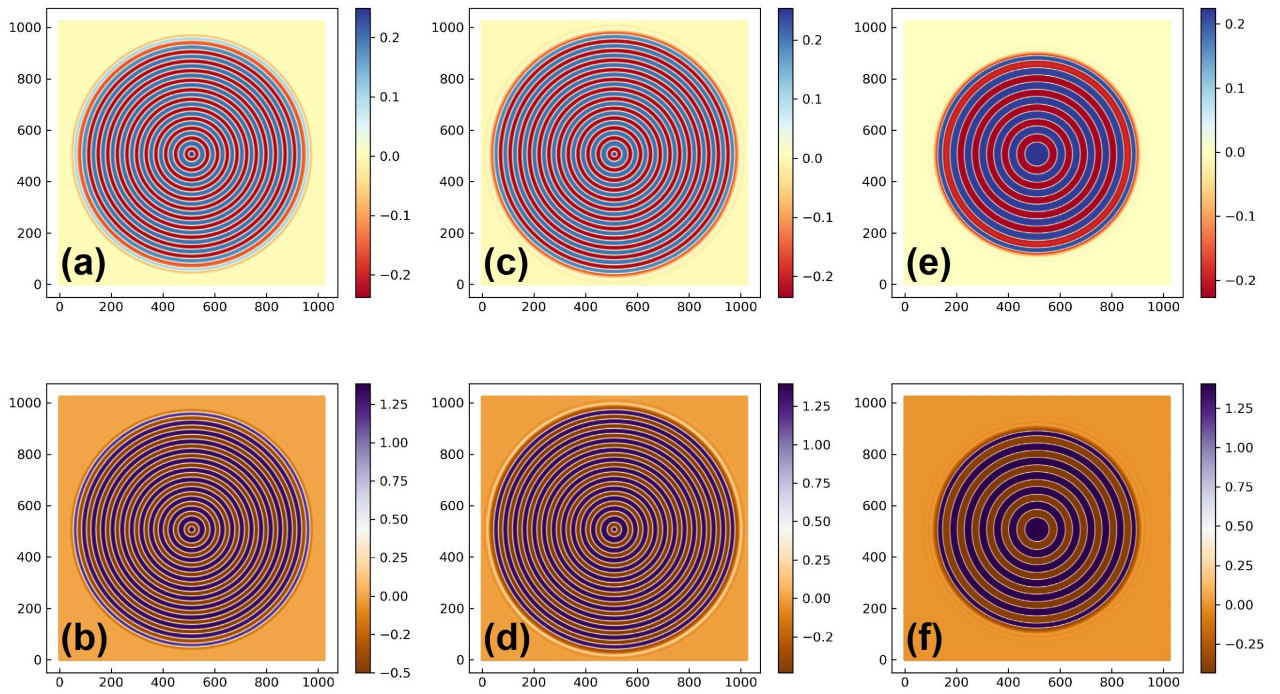


Figure S6: **Simulated banded spherulite patterns.** Numerical solutions of ϕ (upper row) and ψ (lower row) for different values of α (or ΔT). (a, b) $\alpha = 0.250$ ($\Delta T = 40.8$ K) at 149999 time steps, (c, d) $\alpha = 0.300$ ($\Delta T = 38.1$ K) at 199999 time steps, (e, f) $\alpha = 0.450$ ($\Delta T = 29.9$ K) at 399999 time steps on a 1024×1024 square lattice.

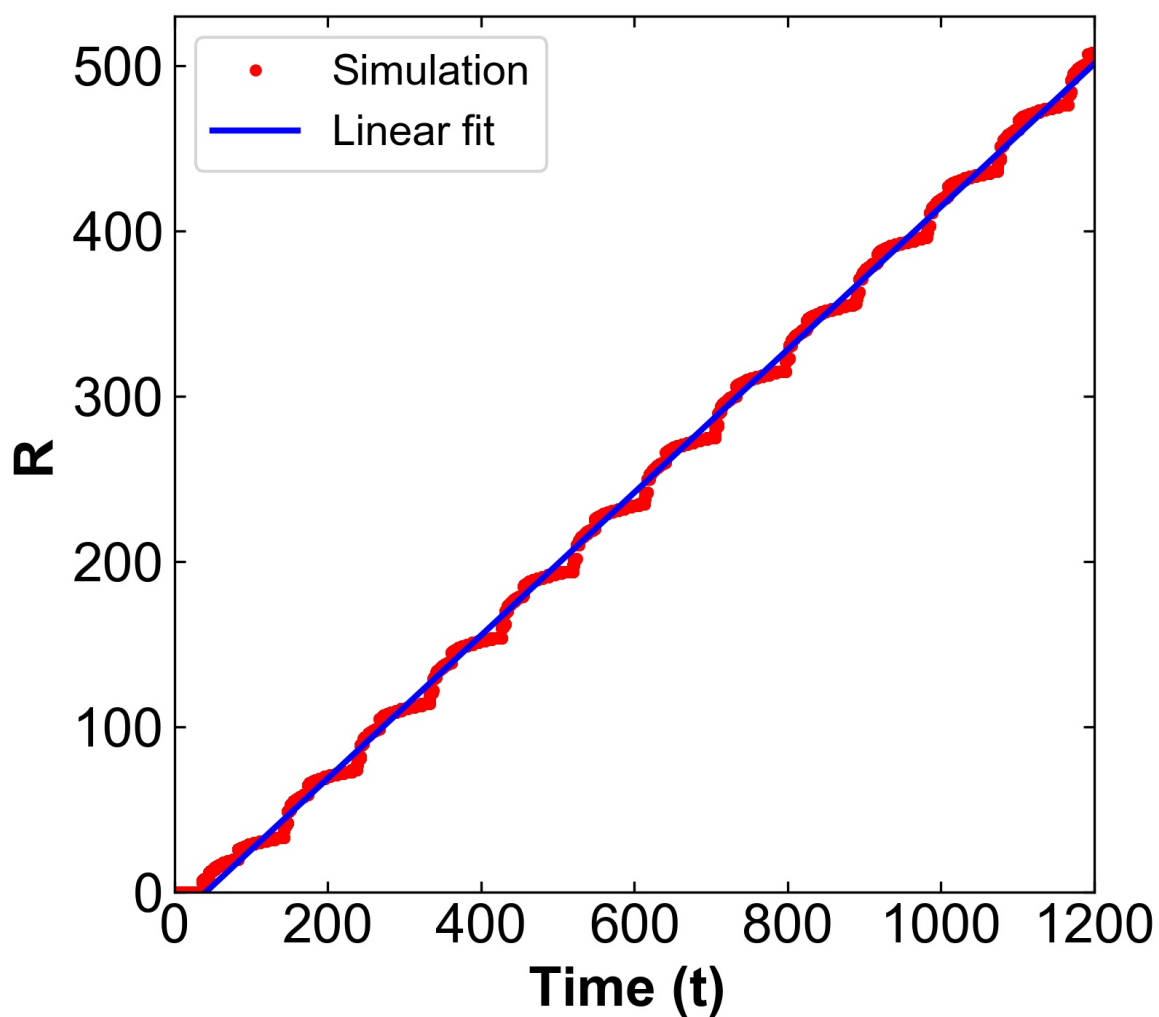


Figure S7: **Rhythmic variation of spherulite radius.** Numerically computed variation of radius R of the banded spherulite with time showing its rhythmic growth for $\alpha = 0.15$ ($\Delta T = 46.3$ K). The blue line shows the average linear growth of the spherulite with time. R and t are dimensionless quantities.

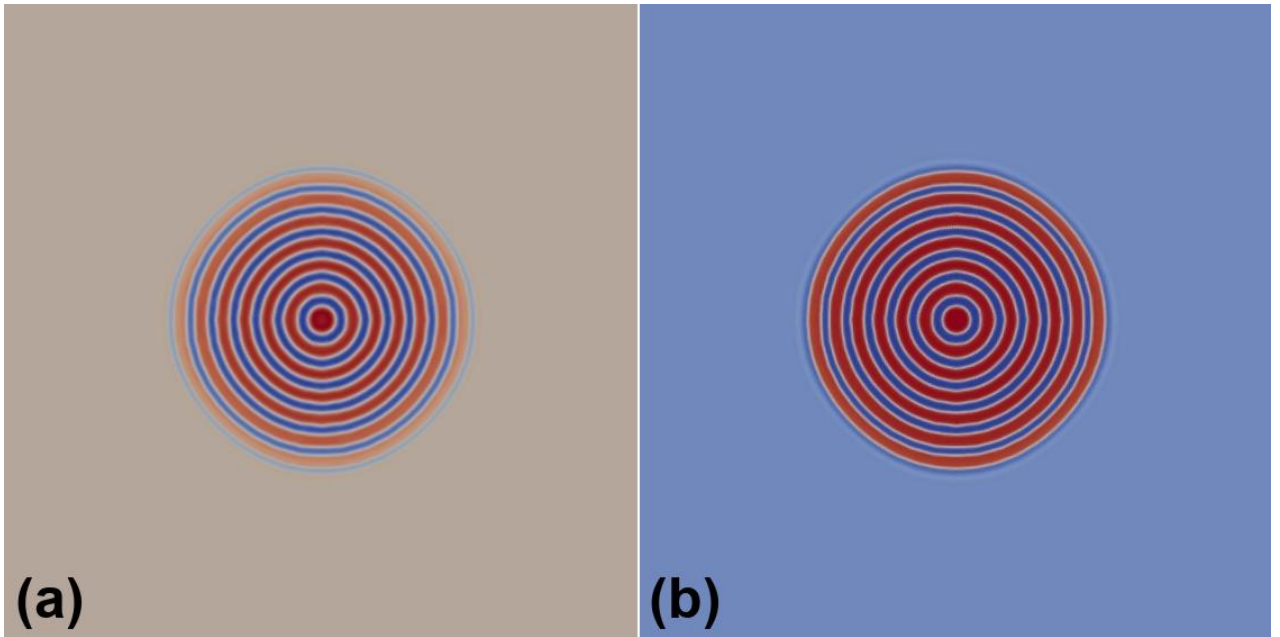


Figure S8: **Banded spherulite patterns by FEM.** The numerical solutions of (a) ϕ and (b) ψ obtained from FEM at 2000 time steps. The parameter values used for the calculations are $\alpha = 0.2$, $\gamma/A = 0.95$, $\xi_\psi/\xi_\phi = 0.5587$, $\xi_\phi^2/\lambda_D^2 = 20.5$ and $W/A = 2.05$.